Applied Surface Science 255 (2009) 4503–4511

Contents lists available at ScienceDirect

Applied Surface Science

journal homepage: www.elsevier.com/locate/apsusc

Processing for optically active erbium in silicon by film co-deposition and ion-beam mixing

S. Abedrabbo [a,*], Q. Mohammed [b], A.T. Fiory [c]

[a] Department of Physics, University of Jordan, Amman 11942, Jordan
[b] Tadawul Shares and Bonds Mediation L.L.C., Dubai, United Arab Emirates
[c] Department of Physics, New Jersey Institute of Technology, Newark, NJ 07901, United States

ARTICLE INFO

Article history:
Received 3 June 2008
Received in revised form 4 November 2008
Accepted 22 November 2008
Available online 30 November 2008

PACS:
85.40.Sz
85.40.Ry
61.80.Jh
61.72.sd
68.55.at
78.55.Hx

Keywords:
Erbium optoelectronics
Ion-beam processing
Enhanced diffusion

ABSTRACT

Techniques of film deposition by co-evaporation, ion-beam assisted mixing, oxygen ion implantation, and thermal annealing were been combined in a novel way to study processing of erbium-in-silicon thin-film materials for optoelectronics applications. Structures with erbium concentrations above atomic solubility in silicon and below that of silicide compounds were prepared by vacuum co-evaporation from two elemental sources to deposit 200–270 nm films on crystalline silicon substrates. Ar^+ ions were implanted at 300 keV. Oxygen was incorporated by O^+-ion implantation at 130 keV. Samples were annealed at 600 °C in vacuum. Concentration profiles of the constituent elements were obtained by Rutherford backscattering spectrometry. Results show that diffusion induced by ion-beam mixing and activated by thermal annealing depends on the deposited Si–Er profile and reaction with implanted oxygen. Room temperature photoluminescence spectra show Er^{3+} transitions in a 1480–1550 nm band and integrated intensities that increase with the oxygen-to-erbium ratio.

© 2008 Elsevier B.V. All rights reserved.

1. Introduction

Erbium plays a dominant role in amplifiers for optical communications because its strong radiative de-excitation transition at 1.5 μm is an excellent match to the corresponding wavelength band of low optical absorption in silica fibers. Erbium-doped fiber amplifiers (EDFA) are heavily utilized to maintain the integrity of signals transported throughout wide area [1,2], metropolitan, and local optical networks [1,3,4]. More recently, erbium doped waveguide amplifiers have been deployed for lower-cost solutions in near-to-access regions [5,6]. Optical sources continue to rely on III–V semiconductor compounds, e.g., InP and GaAs, owing to their excellent electro-optical properties, despite their high processing cost [7]. It is therefore logical that Er–Si structures are being sought for solid-state light sources in this important wavelength range, as part of a broader quest for efficient light sources that are based on silicon and operate at room temperature [8–13]. Optical sources based on Er–Si would importantly leverage the already extensive capabilities of silicon electronics [14]. The achievement of efficient room temperature light emission from crystalline silicon is a crucial step toward the realization of fully Si-based optoelectronics. Achieving a high efficiency silicon light-emitting diode (LED) will enable the replacement of III–V sources in a diverse commercial market for such devices [15].

A variety of methods to incorporate Er and other rare-earth elements in Si have been investigated in order to improve its light emission properties. The most promising techniques generally use processes that are compatible with very large scale integration (VLSI) electronics fabrication and therefore address needs for efficient and low-cost alternative light sources in the communication industry and elsewhere. Many issues arise when incorporating Er in Si, however, the most notable being a high segregation ratio and the low solubility of Er in Si. Some success in circumventing these limitations has been reported, principally through the utilization of ion implantation and solid phase epitaxy [16–19], and film deposition by molecular beam epitaxy [20,21] or chemical vapor deposition [22]. Er–O complexes were sought owing to their effect of enhancing the solubility of Er in Si [16]. Optical activation at 1.5 μm has also been observed for

* Corresponding author. Fax: +962 6 534 8932.
E-mail addresses: sxa0215@yahoo.com, sxa0215@njit.edu (S. Abedrabbo).

0169-4332/$ – see front matter © 2008 Elsevier B.V. All rights reserved.
doi:10.1016/j.apsusc.2008.11.058

silicon-crystal nanowires either coated with Er–Si layers [23] or embedded in Er-doped silica [24].

Related to the optoelectronics applications of Er in silicon, which are the focus of this paper, are studies of erbium disilicide (e.g., orthorhombic $ErSi_{1.7}$) Schottky-barrier contacts on silicon [25–29]. Metallic silicide contacts have been formed by techniques of metal film deposition or ion implantation, followed by silicidation reactions driven by thermal and ion-beam assisted processes. The interest of this paper is to explore Er concentrations that fill in the gap left by previous studies, i.e., in between the dilute dispersions of Er in Si in the optoelectronic materials and the high Er concentration in erbium–silicide compounds.

This work presents results obtained by applying multiple processing methods to achieve Er concentrations that are above the nominal solubility levels of Er in Si. Novel to this work is the use of co-evaporation in vacuum of Si and Er to prepare a precursor Si:Er film by physical vapor deposition on silicon. The subsequent processing steps are irradiation by energetic Ar^+ ions to form a metastable disordered Si–Er alloy, O^+ ion implantation to provide a precursor to internal oxidation, and thermal diffusion to form Si:Er:O structures on Si. The intent of the ion-beam mixing and oxygen implantations is to induce a spread in crystal field environments and thus suppress mutual coupling among the Er ions that could otherwise compete with 1.5-μm optical transitions.

2. Experimental procedure

Two sets of samples were prepared for this study, denoted as A and B, by co-deposition of Er and Si films on silicon substrates in a vacuum chamber equipped with separately controllable resistively heated evaporation boats. Films for sample set A were grown with a buried Si layer to determine the influence of ion-beam mixing and Er–Si interdiffusion. Films for sample set B were grown with a Si cap to ascertain its utility in suppressing post-deposition process loss of Er. The Er boat was charged with the rare earth metal as purified by distillation. The Si boat was charged with p-type Si crystals cut from substrate material. The substrates for each sample sets were 1-cm square sections cleaved from double-side polished wafers of p-type doping (10^{15} cm^{-3} boron), ⟨1 0 0⟩ orientation, 250 μm thickness, and native oxide surfaces. Erbium–silicon composite films were grown to nominal thicknesses of 200 and 270 nm by co-evaporation under a typical chamber pressure of 10^{-4} Pa onto the Si substrates, which were heated to 300 °C. Temperature was determined by a thermocouple attached to the heater block. Elevated deposition temperature was used to promote coalescence of Si and Er in the growth of Si:Er films. Evaporation rates, which ranged from 1.2 to 2.4 nm/s, were monitored by a quartz crystal microbalance detector using an interpolated mass density for the Si–Er film. The ratio of erbium to silicon fluences was in the range of 1:3 to 1:4. Based on the background pressure in the chamber, film deposition rates, and gas sticking coefficients ≤1, less than 5% of the films could comprise constituents absorbed from the chamber ambient.

Sample set A was prepared by varying the Er fluence to produce a three-layer modulation-doped structure in a 270-nm deposited film, as illustrated schematically in Fig. 1a. The full Er and Si fluences were used to deposit the first and third layers, while a mostly Si fluence was used to deposit the second, or middle layer. Modulation in the deposition ratio of Er to Si was achieved by reducing the Er fluence for the middle layer by lowering the temperature of Er boat for less than 30 s and then raising it again. The deposited film structure, comprising Si:Er_x, Si, and Si:Er_y layers of respective thicknesses 120, 50, and 100 nm, and with Er fractional concentrations of x = 0.2 and y = 0.5, was determined by Rutherford backscattering spectrometry (RBS), as discussed in Section 3.

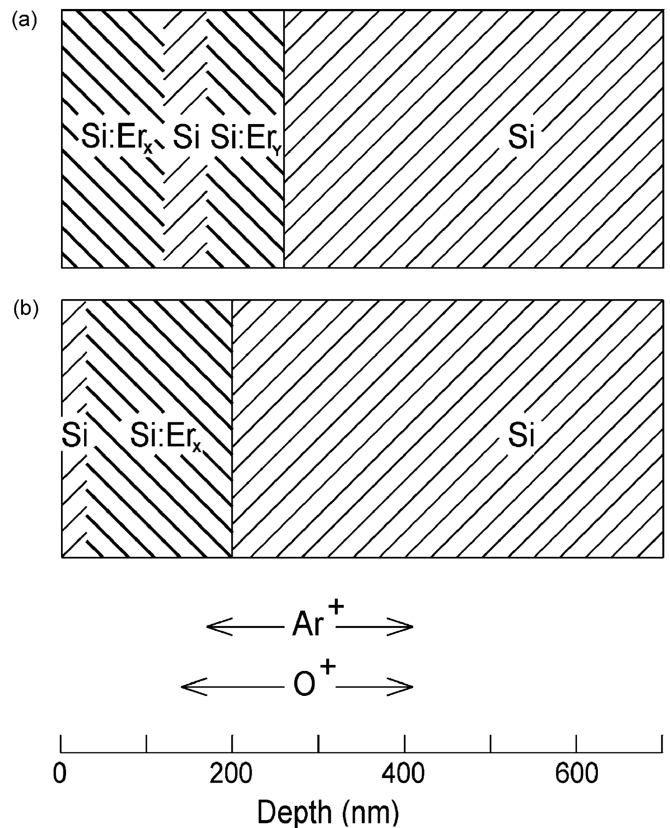

Fig. 1. Structure of films deposited on Si for sample sets (a) A and (b) B. Ranges of Ar^+ and O^+ implants, from $R_P - \Delta R_P$ to $R_P + \Delta R_P$, are denoted by double-headed arrows.

In the preparation of sample set B, the full Er and Si fluences were used to deposit a Si:Er_x film of thickness 170 nm with average Er fraction of x = 0.33. The Si:Er film was then capped with a 30 nm thick Si film, yielding a 200 nm structure comprising Si and Si:Er_x layers on the crystalline silicon substrate, as illustrated in Fig. 1b.

The buried Si layer incorporated in sample A acts as a member of a diffusion couple wherein intermixing of Si and Er can be readily determined. The Si cap layer on sample B serves as a protective mask for knock-on implantation, a buffer for surface segregation of Er, a surface passivation or sacrificial layer during thermal annealing, and also a diffusion couple member.

Control samples from groups A and B, denoted A1 and B1, respectively, were annealed under vacuum at 600 °C for 1 h and reserved for subsequent analysis. Other samples, denoted A2 and B2, respectively, received ion-beam irradiation prior to receiving identical thermal annealing. Structural defects were introduced in samples A2 and B2 using a beam of mono-energetic Ar^+ ions provided by the University of Jordan Van de Graaff accelerator (JOVAC) described in detail elsewhere [30]. The incident energy of the ions was 300 keV, while the fluence (dose) was 1 × 10^{18} ions/cm^2. The samples were further implanted with O_2^+ ions at 260 keV and fluence of 5 × 10^{17} ions/cm^2, which is equivalent to implanting O^+ at 130 keV and 1 × 10^{18} cm^{-2} dose. The radiation doses were applied to 9-mm^2 areas.

Projected ranges, R_P, and range straggles, ΔR_P, of implanted ions were estimated from the stopping powers of Si and Er and an effective medium approximation for Si:Er in the ratio of 4 to 1 [31]. For 300-keV Ar^+ ions one obtains R_P = 290 nm and straggle ΔR_P = 120 nm. The depths of the implanted Ar^+ ions, as determined from the limits of $R_P \pm \Delta R_P$, varies from 170 to 410 nm and is

indicated by the double arrow marker in Fig. 1. The Ar^+ implant extends the depth of the Er atoms by knock-on collisions. The energy of the O^+ ions was chosen such that R_P = 280 nm and ΔR_P = 135 nm, giving an implanted range from 140 to 410 nm that is also indicated by double arrows in Fig. 1.

For both sample sets, the ions are implanted to depths that extend beyond the depth of the deposited Er distribution. One notes from Fig. 1 that the thicker film of sample set A yields higher implant doses within regions containing Er, when compared to sample set B. The differences in film thicknesses, Si–Er structures, and overlap between the Er and implant distributions allows one to determine the interdiffusion of Er, O, and Si induced by ion-beam mixing and internal oxidation from implanted argon and oxygen, respectively.

The Ar implant was chosen to be of sufficient dose and range so as to produce ion-beam mixing throughout the deposited films as well as creating an adjacent amorphized silicon layer in the substrate. Thus the ion-beam mixing effect is expected to be comparable for the two film thicknesses. Moreover, a significant amount of amorphized Si material is made available in both cases for solid phase reaction upon annealing.

The oxygen was implanted in the region previously disordered by the Ar implant, rather than centering it at the Er depth, in order to study the Er–O solid phase reaction and the formation of optically active Er^{+3} centers. Of particular interest is the role of oxygen implanted in the amorphized Si substrate material, where it may serve as a source for internal oxidation of the Er by solid phase diffusion and reaction. Assuming a good admixture of Er in Si, the proximity of the oxygen implant is expected to promote the formation of Si:Er:O complexes upon thermal annealing.

Quantitative analysis of the Er, Si, and O profiles were determined by RBS analysis. Compositions of all samples were determined by the JOVAC RBS facility using a 2 MeV He^+ beam that probed a 1 mm $\times$ 1 mm area (lying within the implanted areas in the cases of samples A2 and B2). The backscattering energy resolution of the spectrometer is 1.908 keV per channel. The detector resolution is 33 keV, which provides a depth resolution of approximately 16 nm in silicon. The He^+ dose was selected to produce a backscattering yield of about 1000 counts per channel in the region of the Er backscattering energy (1.9 MeV). For analysis, RBS spectra were normalized to a constant He^+ dose. The RBS spectra were fitted by simulating the samples as multiple layers of multiple compositions on a silicon substrate. The concentrations of the constituent species, Si, Er, O, and Ar, and thicknesses of the layers were varied to provide a best fit of simulated to experimental RBS spectra [32]. Species volume concentrations and the scale of physical thickness obtained from RBS analysis are referenced to the atomic densities of Er and Si in proportion to their respective concentrations. Carbon was not included in the model, since C peaks were not resolved in the RBS spectra (e.g., the RBS spectra do not resolve any C surface peaks).

A model Flourolog-3 spectrofluorometer was utilized to measure photoluminescence (PL) and optical emission of the samples both before and after irradiation, courtesy of Horiba Jobin-Yvon (Edison, New Jersey). A Xe lamp fixed at 532 nm was used for excitation and a 2-mm Hamamatsu InGaAs photodiode detector determined signal intensity. Photoluminescence intensity was determined by detector photo voltage as a function of luminescence wavelengths from 1400 to 1600 nm.

3. Experimental results

Data are presented for analysis of film composition and diffusion obtained from RBS spectra and the presence of optically active Er obtained from analysis of photoluminescence spectra. The results show that ion irradiation leads to enhanced diffusion in the subsequent thermal annealing step. The present method may be contrasted with previous studies of radiation-enhanced diffusion that are typically isothermal processes [33].

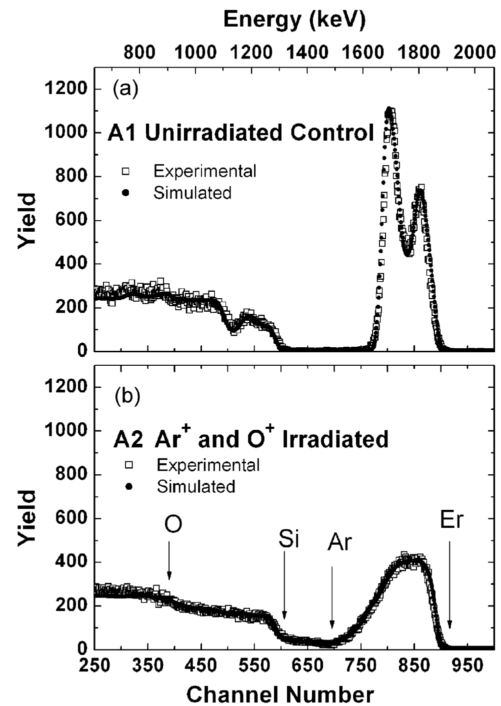

Fig. 2. RBS spectra of (a) unirradiated control sample A1 and (b) irradiated sample A2. Open symbols are measurements, filled symbols are numerical simulations. Arrows mark backscattering energies of surface O, Si, Ar, and Er.

3.1. RBS analysis

Experimental and simulated RBS spectra are shown in Fig. 2 for the unirradiated control sample, A1, and the irradiated sample, A2. Arrows denote the maximum energies of He^+ backscattering from O, Si, Ar, and Er at 915, 1302, 1470, and 1902 keV, respectively (channels 394, 598, 686, and 913, respectively), which correspond to backscattering from the surface. The presence of oxygen is revealed by a small step at the O surface edge. Backscattering from Ar in the irradiated sample A2 produces yields in the energy region between backscattering from Si and Er.

A prominent feature of the spectrum for the non-irradiated control A1 is the doubled peak structure corresponding to backscattering from Er in the two erbium-containing layers in the modulation-doped film structure. Related to this is the pronounced modulation that is observed in the backscattering spectral yield from Si in the film. The RBS analysis thus reveals that a modulation-doped structure (Fig. 1a) is retained in unirradiated sample A1 after the thermal annealing treatment.

The spectrum for the irradiated sample A2 shows a single broadened Er peak and a monotonic Si spectrum. Broadening of the Er peak, observed as a decrease in peak height by 30% and an increase in peak width, when compared to the spectrum for sample A1, is attributed to species intermixing and diffusion. Comparison between the spectra for A1 and A2 shows no difference in the maximum backscattering energy from Er, indicating that sample A2 is smoothly doped with Er right up to the surface. The low energy tail of the Er portion of the spectrum for A2 indicates that, as a consequence of post-irradiation enhanced thermal diffusion, the Er distribution is driven into the silicon substrate.

Fig. 3 shows RBS spectra for the unirradiated control sample B1 and the irradiated sample B2, overlaid with simulated spectra.

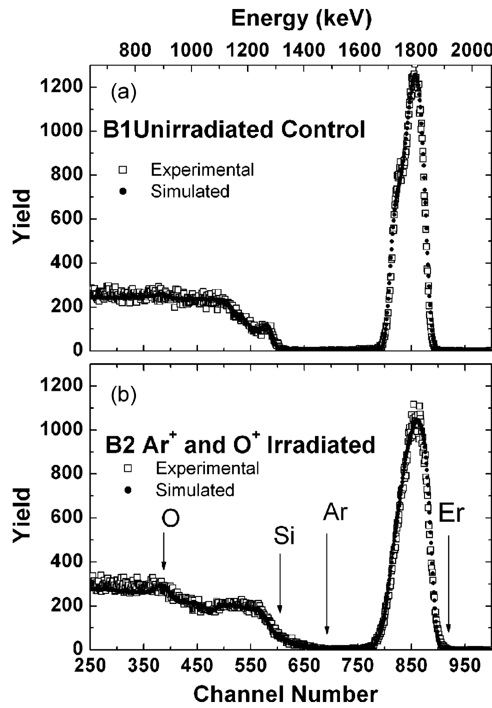

Fig. 3. RBS spectra of (a) unirradiated control sample B1 and (b) irradiated sample B2. Open symbols are measurements, filled symbols are numerical simulations. Arrows mark backscattering energies of surface O, Si, Ar, and Er.

Samples from group B were prepared with a Si cap film over a nearly uniform Si:Er_x layer. The Er backscattering peak in the spectrum of Fig. 3a for control sample B1 shows minor structure (slight shoulder), in contrast to the doubled Er peaks for control sample A1 (Fig. 2a). The effect of the Si cap appears in the spectrum for sample B1 as a surface peak in the backscattering from Si. There is also a corresponding shift in the maximum energy of backscattering from Er towards lower energy by about 20 keV, when compared to, e.g., the spectrum for control sample A1. This confirms that a Si:Er_x film remains buried in the control sample B1, even after thermal annealing. Backscattering from Er in the irradiated sample B2 shows that Er has diffused into the Si cap as well as the Si substrate. Thus the thinner films of sample set B also show the effect of post-irradiation enhanced thermal diffusion. On comparing Figs. 2 and 3, one notes that the irradiation-induced diffusion broadening of the Er distribution is larger in the thicker (A2) film.

On comparing Fig. 2a and b, it appears that the Er yield in the RBS spectra for irradiated sample A2 is reduced when compared to unirradiated sample A1. In contrast, the Er yields for irradiated sample B2 and unirradiated sample B1 appear to be similar (Fig. 3). Reductions in Er yield are attributed to film sputtering by the ion beam irradiation. Less Er is lost for sample B2, which has the Si cap layer. Er yield results are determined quantitatively in the RBS analysis given below.

The filled points in Figs. 2 and 3 display the four simulated RBS spectra that were fitted to the experimental data. Differences between simulation and experiment have been minimized (except for deep backscattering in the Si substrate), ascertaining accuracy in the fitting procedure.

Layer by layer simulation fitting of the experimental RBS spectra were used to obtain depth profiles of the various elements. The number of layers in the simulations (14, 19, 7, and 14 layers for samples A1, A2, B1, and B2, respectively), was selected to give similar depth resolution among the various films. Uncertainties in obtaining species concentrations, estimated to be $\pm$ 0.05, arise from statistical noise, fitting correlations between concentration and thicknesses in the layers, and experimental uncertainties, principally in He^+ dose, detector resolution, and spectrum calibration. While RBS accurately determines area concentrations of the various atomic species, computation of the depth scale entails uncertainties related to the atomic volumes of the constituent species. For the analysis presented, atomic volumes were interpolated between pure Er and Si. Accuracy of the depth scale is estimated to be better than 10%, based on consideration of more refined models for the presence of Er–O, Er–Si, and Si–O microstructures in the samples and their atomic densities.

A film thickness parameter, d, is defined as the maximum depth of the Er distribution as found from analysis of the RBS simulations. The area concentration of erbium, N_{Er}, is derived by summing the area concentrations in the layers of the simulation, and is given by

$$N_{Er} = \sum_{k=1}^{n} N_{Er}(k), \qquad (1)$$

where the index k denotes a layer in the simulation and $N_{Er}(k)$ is the Er area concentration in layer k. The layer for $k = n$ is at the maximum depth of the Er distribution, i.e., at depth d. Depth profiles of the fractional concentration of the constituent elements in the simulations were computed as

$$C_p(k) = \frac{N_p(k)}{\sum_p N_p(k)}. \qquad (2)$$

Here, the index p refers to the atomic species (Si, Er, O, or Ar) in layer k of the simulation and $C_p(k)$ is the fractional concentration of species p in layer k. Fractional concentrations as obtained from Eq. (2) are shown as functions of depth for sample sets A and B in Figs. 4 and 5, respectively. Average fractional concentrations of the elements within the depth d are determined as

$$\langle C_p \rangle = d^{-1} \sum_{k=1}^{n} t(k) C_p(k), \qquad (3)$$

where $t(k)$ is the thickness of layer k in the simulation. By identity, we have $d = \sum_k t(k)$. Results obtained from Eq. (3) are thus denoted as $\langle C_{Si} \rangle$, $\langle C_{Er} \rangle$, $\langle C_O \rangle$, and $\langle C_{Ar} \rangle$. Film thickness, Er area concentrations, and fractional concentrations obtained from the simulations are given in Table 1.

On comparing results for samples A1 and A2 (Table 1 and Fig. 4) one observes an increase in the depth of the Er distribution from d = 268 nm in unirradiated sample A1 to d = 524 nm in irradiated sample A2. The increase in film thickness parameter by a factor of 2.0 shows that the redistribution of Er by thermal diffusion is enhanced by the ion-beam processing. In addition, RBS analysis finds that ion-beam irradiation leads to a decrease of N_{Er} (area concentration) from 172 to 117 $\times$ 10^{15} cm^{-2}. This loss of about one-third of the deposited Er is attributed to ion-beam sputtering of the film, even though the Si:Er film of irradiated sample A2 is thicker than that of control sample A1. This supports the interpretation that the low energy tail in the Er portion of the RBS spectra from sample A2 (see Fig. 2b) arises from ion-beam

Table 1
Film thickness (defined as depth of Er distribution), d, Er area concentration, N_{Er}, and average fractional concentrations of elemental species Si, Er, O, and Ar in unirradiated (A1, B1) and irradiated (A2, B2) samples, as determined from fitted simulations of RBS spectra. Parameter σ is the square-root of the spatial variance in Er concentration distribution, as determined from Eq. (6).

Sample	d (nm)	N_{Er} (10^{15} cm^{-2})	$\langle C_{Si} \rangle$	$\langle C_{Er} \rangle$	$\langle C_O \rangle$	$\langle C_{Ar} \rangle$	σ (nm)
A1	268	172	0.56	0.15	0.29		79
A2	524	117	0.72	0.05	0.14	0.10	112
B1	199	164	0.65	0.22	0.13		44
B2	285	153	0.66	0.12	0.13	0.08	56

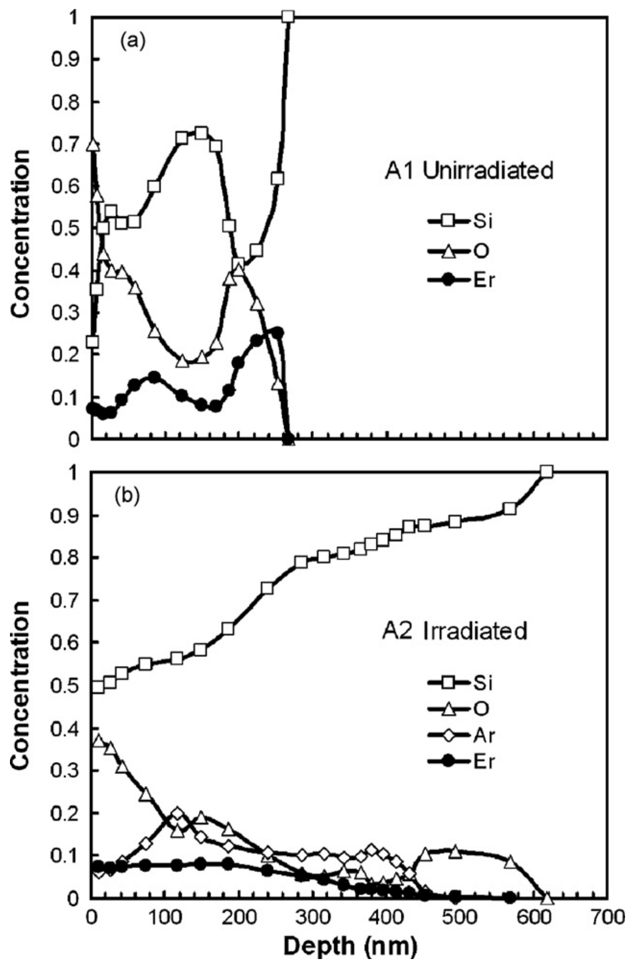

Fig. 4. Fractional concentration distributions of atomic species in (a) unirradiated control sample A1 and (b) irradiated sample A2.

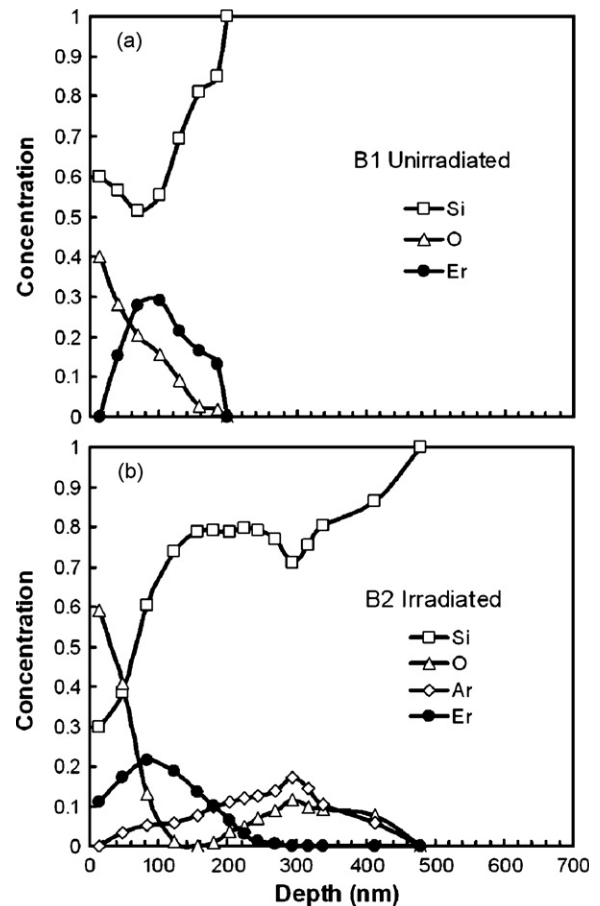

Fig. 5. Fractional concentration distributions of atomic species in (a) unirradiated control sample B1 and (b) irradiated sample B2.

induced diffusion, as opposed to effects of film thickness uniformity.

The Er profiles for samples B1 and B2 shown in Fig. 5 show that ion-beam irradiation allows Er to migrate into the Si cap as well as into the Si substrate and leads to an increase in the depth of the Er distribution by approximately a factor of 1.4. This confirms that ion-beam mixing effects extend up to the surface. Ion-beam irradiation has thus also produced a noticeable enhancement in the thermal diffusion of Er in the thinner films of sample set B. Owing to the Si cap in the group B samples, the retained Er concentration is 93%, in contrast to the 67% retention for the uncapped Si:Er film of group A. The thickness of the cap, as determined by RBS for sample B1, is 28 nm, which appears sufficient to largely suppress loss of Er by sputtering and out diffusion.

Oxygen concentration profiles shown in Figs. 4 and 5 indicate oxidation of some portion of the Er in all samples. Since oxygen profiles near the surface have similar shape (similar penetration depths of about 100 nm), it appears that part of the Er oxidation arises from uptake of oxygen from the ambient during film processing.

3.2. Optical analysis

Room temperature photoluminescence (PL) spectra for samples A1 and A2 are shown in Fig. 6 and for sample B1 in Fig. 7. As the PL appears to have been replicated in irradiated sample B2, the spectrum for only B1 is shown.

The PL spectra reveal that the host matrix induces odd-parity character in perturbed Er 4f wave functions, thereby allowing radiative transitions to be observed. Noting that the deposition temperature was 300 °C, A2 was further irradiated, and that the annealing temperature was 600 °C clearly indicates that the resulting structures are at best polycrystalline with small grain sizes. Thus, Er ions may occupy more than one atomic site, or activator center, in the host matrix. Different sites will possess different symmetry and hence different crystal fields which will yield randomization to the Stark splitting effect of the $^4I_{13/2}$ and $^4I_{15/2}$ levels of Er. This will produce inhomogeneous broadening and forms an emission band spanning wavelengths from 1480 to 1560 nm [34–36]. In addition, the presence of appreciable concentrations of oxygen in the present samples, as determined from the RBS analysis (Table 1), and the 600 °C one-hour annealing process should make the multi-crystalline structure loosely similar to a glassy network. This interpretation is consistent with the results found for samples A1 and A2, apart from differences in peak wavelengths and spectral shape. Thus we apply the same analysis method as in Ref. [34] and model the PL spectra as a superposition of spectral transitions at multiple wavelengths. The functional form of the PL intensity is expressed as a linear combination of Gaussian peaks:

$$I(\lambda) = I_0 + \sum_{k=1}^{n} \sqrt{\frac{2}{\pi}} \frac{A_k}{w_k} \exp[-2(\lambda - \lambda_k)^2 / w_k^2], \quad (4)$$

where I_0 is a baseline, n is the number of fitted transitions in the PL band, and k is the index of a transition peak of relative area A_k,

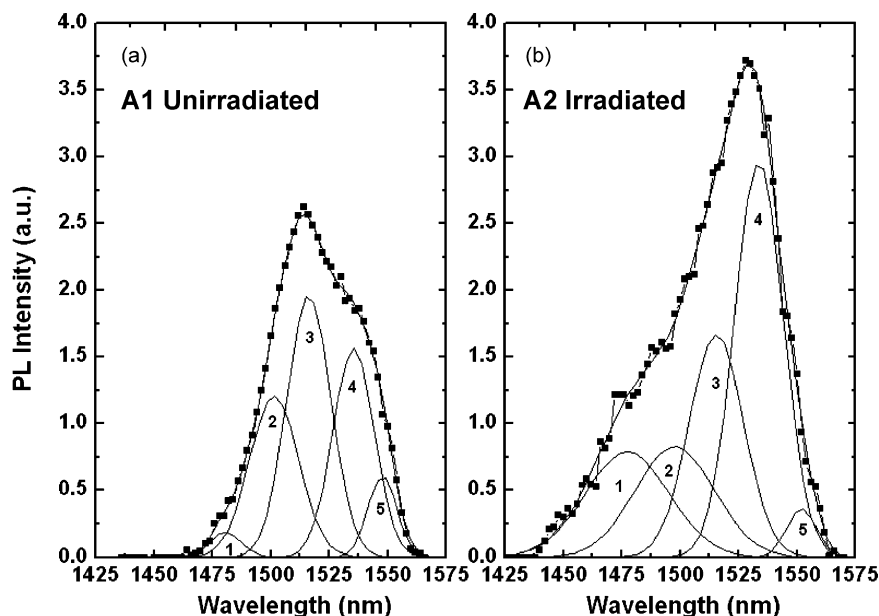

Fig. 6. Photoluminescence spectra of (a) unirradiated control sample A1 and (b) irradiated sample A2. Numbered peaks are fitted Er transition components (Table 2).

width w_k, and wave length λ_k. We find that the Gaussian line shape model given in Eq. (4) provides good fits to the PL spectra.

The PL spectra were fitted with various values of n from 2 to 8. However, for samples A1 and A2 a model for $n = 5$ yields not only a good fit but also determines a set of λ_k that are traceable to possible transitions between the first excited state $^4I_{13/2}$ to the ground state $^4I_{15/2}$ of the spin-orbit and Stark split Er 4f level in aluminosilicate-glass [34,36]. Initial guesses in the fitting procedure used wavelengths of 1480, 1500, 1515, 1533, and 1550 nm. The parameters in Eq. (4) were then varied to obtain the best fit. The authors admit however, that by no means are these wavelengths unique, but they are indicative of the similarities of the processed samples and glassy-networks as briefed above. Examining the fitted wavelengths in comparison to the allowed transitions in Ref. [34], one notes that they correspond, respectively, to the maximum energy typically permitted by the $^4I_{13/2}$–$^4I_{15/2}$ transition, and to transitions from 6644 to 0 cm^{-1} (wave numbers are referenced to the lowest Stark level in the $^4I_{15/2}$ manifold), 6640 to 51 cm^{-1}, 6644 to 133 cm^{-1}, and 6711 to 268 cm^{-1}. Results for the component peaks are shown in Fig. 6. Wavelengths, widths, and relative intensities determined from areas under the peaks (expressed as percentages with respect to the total spectra area) are given in Table 2.

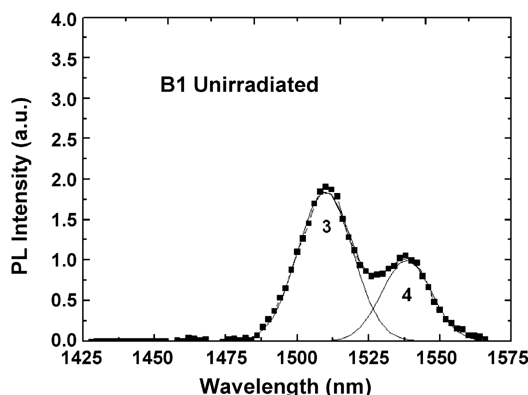

Fig. 7. Photoluminescence spectra of sample B1. Numbered peaks are fitted Er transition components (Table 2).

When the PL spectra of A1 and A2 are compared, we find that irradiation leads to a 62% increase in the PL intensity (determined by the area under the PL spectra), even though 32% of the Er is lost through sputtering and the volume concentration of the remaining Er is reduced by enhanced diffusion broadening. Irradiation also changes the wavelength of the strongest peak, as determined by the resolved peak of largest area in the fitting, which can be explained as the creation of new dominant transitions due possibly to irradiation induced shifts to the dominant Er atomic site symmetry in the excited (illuminated) area. In A1 it is clear that 1516 nm is a dominant transition while the most intense transition in A2 is at 1533 nm. It is also important to note that the transition of the highest energy at 1480 nm is negligible in A1 while it becomes appreciable in A2. The increase in PL intensity with irradiation was also examined by subtracting the PL spectra of sample A1 from that of A2. The difference spectrum (not shown) has maxima at wave lengths of 1480 and 1533 nm, which is consistent with the results of the Gaussian-peak fitting model.

A model with $n = 2$ yields a good fit to the PL spectra of B1, which is narrower and clearly has fewer components than either A1 or A2. The fitted peaks are shown in Fig. 7 and the fitting parameters are given in Table 2. It is notable that the spectrum for B1 is very similar to the emission spectra exhibited by Er in silica-based fibers and with semi-insulating polycrystalline Si doped with Er [36,37]. For the two capped samples B1 and B2, loss and redistribution of Er are minimal and most of the implanted oxygen stopped in the substrate and beyond the depth of the deposited film. Hence the optical activity of the Er remains largely the same.

Table 2
Er transition peaks fitted to photoluminescence spectra for samples A1, A2, and B1. Peak numbers correspond to fits according to Eq. (4) and shown in Figs. 6 and 7. λ is peak wavelength, A is percentage area under peak, w is width.

Peak No.	A1			A2			B1		
	λ (nm)	A (%)	w (nm)	λ (nm)	A (%)	w (nm)	λ (nm)	A (%)	w (nm)
1	1480.7	2.6	13.2	1477.4	17.5	35.8	–	–	–
2	1501.5	25.4	25.4	1497.7	17.3	33.9	–	–	–
3	1516.3	36.9	18.9	1515.5	24.0	23.4	1509.8	67.0	19.0
4	1535.4	27.6	17.6	1533.6	38.4	21.0	1538.3	33.0	17.1
5	1547.7	7.5	12.3	1551.9	2.8	12.5	–	–	–

4. Discussion

The redistribution of Er and the photoluminescence spectra are discussed in terms of the deposited film structure and the effects of ion-beam irradiation.

4.1. Er redistribution

While the 1-h anneals at 600 °C of this study may be sufficient for silicon recrystallization, the corresponding thermal budget is generally insufficient for observing conventional concentration-dependent diffusion. The Er profiles obtained for the unirradiated samples A1 and B1 confirm this picture. However, ion-beam irradiation was found to induce broadening of the Er distribution, as shown in Figs. 4b and 5b. The broader Er profiles in the irradiated samples can thus be attributed to the combined effects of ion-beam irradiation and thermal diffusion.

One may define a characteristic length associated with the Er diffusion as $L_D = \langle Dt \rangle^{1/2}$, where $\langle Dt \rangle$ is an average diffusivity-time product (equivalently, a definition of thermal budget). Using a Gaussian diffusion model, and assuming negligible diffusion in the unirradiated case, one may express the enhanced diffusion length for the irradiated samples in terms of the difference in the variances of the Er depth distributions:

$$L_D^2 = \sigma_2^2 - \sigma_1^2 \quad (5)$$

where σ_1^2 is the variance of the Er distribution for the unirradiated control sample (A1 or B1) and σ_2^2 is the variance for the irradiated sample (A2 or B2). The depth variances are computed from the fitted Er concentration profiles as

$$\sigma_i^2 = \frac{\sum_k x_k^2 N_{\mathrm{Er}}^i(k)}{\sum_k N_{\mathrm{Er}}^i(k)} - \left(\frac{\sum_k x_k N_{\mathrm{Er}}^i(k)}{\sum_k N_{\mathrm{Er}}^i(k)}\right)^2, \quad (6)$$

where index k denotes a layer in the simulated RBS spectrum, length x_k is the distance from layer k to the surface, $N_{\mathrm{Er}}^i(k)$ is the Er concentration in layer k, and index i denotes whether the sample is unirradiated ($i = 1$) or irradiated ($i = 2$). Results for σ for the four samples are given in Table 1. One finds that the σ values for the irradiated samples A2 and B2 are larger than the σ values for respective unirradiated control samples A1 and B1, even though all samples were annealed simultaneously.

Enhanced diffusion lengths determined from Eq. (5) are $L_D = 80$ nm for group A and $L_D = 34$ nm for group B. The difference in L_D between the two sample sets indicates that the effective $\langle Dt \rangle$ increases by a factor of 5.5 for film thickness increase by a factor of 1.35. The enhanced Er diffusion is interpreted below in terms of radiation damage per se in combination with internal oxidation associated with the O implant.

Silicon film depositions at 300 °C generally yield films that are amorphous, i.e., no long-range crystalline order is expected to be present. However, a deposited amorphous film may contain short-range correlations among the constituent species, although they may be difficult to detect. The present findings show that ion-beam mixing enhances the diffusion irrespective of whether the starting materials are either amorphous or crystalline, demonstrating in particular the capability of creating ion-beam damage in amorphous material. Although radiation damage is generally maximum near R_P, the Ar^+ dose used in this study is sufficient to fully amorphize silicon right up to the surface. Thus the Ar^+ implant damage within the Si:Er film is expected to have become saturated. This is confirmed by the redistribution of Er into the buried Si layer of sample A2 and into the Si cap layer of sample B2.

The above findings are also consistent with the Ar distributions shown in Figs. 4b and 5b. The depth of the Ar distribution is found to be 450 nm, which agrees with the estimated $R_P + \Delta R_P = 410$ nm, to within the experimental uncertainty of 10%. Thus Ar irradiation creates similarly amorphized Si layers underneath the Si:Er deposit in both A2 and B2 samples. Consequently, radiation damage by itself appears to be insufficient to fully explain the observation of significant differences in L_D between samples A2 and B2.

Differences in L_D associated with Si:Er film thickness is therefore most likely associated with Er diffusion that is enhanced not only by excess populations of defects produced by ion beam irradiation, but also by proximity to the implanted oxygen. The depth of the Er in the deposited film is closer to the range of the oxygen implant in the case of the thicker film of the A2 sample. From a Gaussian model of the implanted O^+ distribution, one estimates that 46% of the O^+ dose is implanted within the deposited film of sample A2 while it is only 35% for sample B2. From the same model, the Er distributions after annealing overlaps 96% of the initial O^+ implant profile for sample A2 and 50% for sample B2. Thus it appears that about twice as much oxygen is theoretically available for internal oxidation in the thicker A2 film. We therefore conclude that the Er redistribution is assisted by an Er–O reaction that is promoted by the ion-beam damage.

4.2. Er optical transitions

In pure Er metal or free Er^{+3} ions, parity selection rules suppress radiative transitions irrespectively of whether they are induced optically, electrically or thermally. Odd-parity character in perturbed Er 4f wave functions may be introduced in a solid host, provided that Er conglomeration by segregation and precipitation is avoided, thereby permitting weak radiative transitions. For example, the luminescence of Er in crystalline Si is enhanced in the presence of impurities such as O [38]. While Er solubility in Si has been experimentally extrapolated to $\sim 1.4 \times 10^{18}$ cm^{-3} [17], the widely used process of fabricating Si–Er by ion-implantation and high-temperature annealing limits the maximum Er concentration to only $\sim 10^{16}$ cm^{-3} [39]. However, the studies referred to above [25–29] have indicated that Er–Si structures containing Er concentrations above normal solubility levels can be achieved without evidence of appreciable Er–Er reduction. These studies did not even consider O or other precursors that are known to increase Er solubility in Si. The present method of co-evaporation at 300 °C followed by post-deposition annealing at 600 °C, although aimed at a different purpose altogether, essentially mimics a process for forming erbium silicide (~37% Er). The observation of photoluminescence at room temperature implies that while segregation of Er may be favored energetically, it is insufficient to quench the optical activity. As discussed below, one can attribute this to the presence of oxygen in the samples.

Although the formation of Er–O and Er–O–Si complexes are known to contribute to the optical activity of Er, a precise mechanism for light output enhancement due to the presence of O has not been clearly established. Among the possibilities that have been postulated are (a) the concentration of Er in Si is higher in the presence of O impurities due to the formation of localized Er–O complexes, as opposed to optically inactive Er precipitation, and (b) an Er–O ligand complex is formed that provides dipole coupling to channel the energy of the electron–hole recombination to the 4f Er manifold [40]. The latter can be portrayed as an essential role played by the ligand to provide the necessary energy-transfer from silicon band-to-band transitions to Er impurities in order to cause the inversion (excitation) needed for light emission. High electronegativity elements like O are well known to increase the optical activity of Er by means that are not restricted to increasing solid solubility or decreasing Er segregation. When introduced into the solid host, oxygen increases absorption probability and emission yield [41].

The increase in PL intensity of sample A2, when compared to A1, suggests that ion irradiation breaks up Er–Er segregation and creates kinetic barriers to segregation through the combined effects of sputtering, ion-beam mixing, and incorporation of oxygen from the implant. Hence, not all of the Er constituents of A1 are optically active and some may have conglomerated in the form of Er–Er. Thus, one may deduce that more Er ions are optically active in A2 than A1. In addition, thermal annealing also increases the redistribution of the Er. There is a corresponding increase in the O:Er ratio from 1.9 in sample A1 to 2.8 in sample A2 (calculated from Table 1). One may compare these findings to the observation of Coffa et al., who determined an optimum O:Er ratio near 10 for Er–O–Si precipitate phases formed in implanted Si [16]. Looking at the O:Er ratio for samples B1 and B2, we find values that are much lower, 0.6 and 1.1, respectively. The lower O:Er ratio in B1, along with the presence of a Si cap and shallower Er depth, appear to correlate with the observation of lower PL intensity, when compared to samples A1 or A2. Areas under the PL spectra shown in Figs. 6 and 7 systematically increase with O:Er ratio (a nearly linear variation). This trend confirms the picture set forth earlier that the presence of O plays a central role in creating optically active Er in the Er:Si:O structures. Extrapolating a linear fit to the data for B1, A1, and A2, one projects a 30% increase in PL intensity for a unit increase in O:Er ratio.

Previous studies have shown that room temperature photoemission at 1.5 μm may be stimulated from Er^{+3} in both silicon and silica media adjacent to Si nanowire crystals [23,24]. Our findings in light of these prior works lend one to conclude that the present samples possess nanostructures as a result of the IM process. Since the excitation wavelength of 532 nm corresponds to direct absorption at the $I_{15/2}$–$S_{3/2}$ transition, the direct role of nanostructure in the activation, i.e., via photo-excited carriers in Si, remains to be determined. However, the IM process dramatically increases the portion of Er^{+3} ions contributing to the emission, which may be attributed to nanostructure formation and reduced Er–Er segregation.

It is interesting to note that the International Telecommunications Union has adopted the Bellcore specification for the wavelengths serving as conventional band (C-Band) from 1530 to 1565 nm while the short band to span 1460–1530 nm with 100 GHz offset [42,43]. The PL spectra of both A1 and A2 therefore extend beyond the limits of the C-Band. Photoemission at 1480 nm in irradiated sample A2 lies at the edge ($\sim$6760 cm^{-1}) of the permitted $^4I_{13/2}$–$^4I_{15/2}$ allowed transitions in the silica-based Er-doped fibers. However, with intensity extended to shorter wavelengths by irradiation, it is clear that a structure like sample A2 with a proper filter is a candidate for Si-light source for the communications industry at more than one single band.

Irradiation effects change the intensity maxima, as determined by the peak with largest area, from 1516 nm in A1 to 1533 nm in A2. Further study of the dependence on Ar^+ and O^+ implant energies and doses will be needed to firmly establish relationships between ion beam processing and the creation of dominant radiative transitions in Er which maybe linked to Er site symmetry [44]. The objective is to fabricate LEDs with specified operating wavelength.

It should be noted that the strong variation in Er concentration in the processed structures is likely to affect the refractive index, which in turn affects the radiative lifetime according to

$$\tau_{\rm rad}^{-1} = (2.88 \times 10^{-9}) n^2 \frac{\int I(\tilde{\nu}) d\tilde{\tilde{\nu}}}{\int I(\nu) \tilde{\nu}^{-3}\, d\tilde{\nu}} \int \frac{\varepsilon(\tilde{\nu})}{\tilde{\nu}} d\tilde{\nu}, \qquad (7)$$

where $\tau_{\rm rad}$ is the radiative lifetime (s), n is the refractive index, I is the fluorescence emission, ε is the extinction coefficient, and $\tilde{\nu}$ is the frequency (cm^{-1}). [45]. This is a major modification in the environment surrounding the radiative impurity centers which may have an overall effect on measured system characteristics. However, due to our current inability to separate radiative lifetime from both homogeneous and inhomogeneous broadening, we presently cannot quantify those characteristics.

5. Conclusions

In this work, Er was introduced into silicon using the unorthodox combination of co-evaporation, ion-beam mixing, oxygen implantation, and thermal annealing. The study demonstrated that this is a viable pathway for preparing Er concentrations in Si lying above the solubility level in Si and approaching that of the erbium silicides and oxides. High Er content and the presence of oxygen form the basis for obtaining emission in near infrared communication bands. Irradiation effects have been studied in samples with modulation-doped (group A) and Si-capped (group B) Si:Er structures of two thicknesses. While Ar-beam sputtering produces a significant 32% Er loss in the uncapped sample, photoluminescence analysis finds increased optical emission intensity, which can be traced to increased oxygen content. Moreover, the optical spectrum with ion irradiation suggests decreased Er segregation and improved distribution into Si, possibly due to the formation of structures with Er–O bonds by the ion-beam process. Introducing sacrificial Si cap-layer before irradiation reduces the loss of Er to 7%. However, the capped film showed less Er diffusion, when compared to the uncapped modulation-doped film. This is because the capped deposited film was thinner, allowing more of the ion irradiation, particularly the O^+ implant, to pass through. The dependence on film thickness shows that Er redistribution is promoted by reaction with the implanted oxygen.

Photoluminescence shows bands of Er^{3+} transitions between Stark-split $^4I_{13/2}$ to $^4I_{15/2}$ levels. Emission intensities are found to increase systematically with the oxygen-to-erbium ratio. This shows that the Er-O reaction could be optimized by tuning the oxygen implant to place maximum dose within the deposited Si:Er film.

This study demonstrated that creating LEDs with different emission peaks wavelengths is possible and that a tunable LED is feasible. In principle, a tunable laser could be created from such structures exactly as has today's tunable fiber-based lasers based on impurity centers like Er. The present results suggest that further studies of the Er–O–Si microstructure would be of interest in elucidating the nature of the optically active oxygen–erbium that forms at high Er concentrations in silicon. Increased Er content prior to irradiation steps and study of Er precipitation would also be of interest.

Acknowledgments

This work was supported by the assistance of the Deanship of Academic Research at the University of Jordan, Project contract no. 1030 and Hamdi Mango Center for Scientific Research (HMCSR).

The authors are indebted to Professor N.M. Ravindra of New Jersey Institute of Technology for his continuous interest, support and encouragement. We would like to thank the JOVAC accelerator crew, and Professor D.E. Arafah and Horiba Jobin-Yvon fluorescence division in Edison, New Jersey, and the Physics Department at Rutgers University, New Brunswick, New Jersey, for their invaluable assistance.

References

[1] C.-S. Li, F.F.-K. Tong, C.J. Georgiou, M. Chen, INFOCOM '94, Networking for Global Communications, 13th Proceedings IEEE 1, 1994, pp. 130–137.

[2] B. Mukherjee, IEEE J. Sel. Areas Commun. 18 (10) (2000) 1810–1824.
[3] S.S.-H. Yam, Y. Akasaka, Y. Kubota, R. Huang, D.L. Harris, J. Pan, IEEE Photonics Technol. Lett. 16 (2004) 425–427.
[4] B. Ramamurthy, J. Iness, B. Mukherjee, IEEE/ACM Trans. Networking 6 (1998) 755–767.
[5] R.R. Thomson, H.T. Bookey, A.K. Kar, M.R. Taghizadeh, A. Klini, C. Fotakis, F. Romano, A.P. Caricato, M. Martino, S. Shen, A. Jha, Electronics Lett. 41 (2005) 1376–1377.
[6] R.R. Thomson, H.T. Bookey, N. Suyal, A.K. Kar, Appl. Phys. Lett. 89 (2006) 101–108.
[7] S. Koehl, M. Paniccia, The quest to siliconize photonics, Photonics Spectra November (2005) 53–60.
[8] D.J. Lockwood, Light emission in silicon, in: D.J. Lockwood (Ed.), Light Emission in Silicon from Physics to Devices. Semiconductors and Semimetals Series, vol. 49, Academic Press, Chestnut Hill, MA, 1998, p. 6, Chapter 1.
[9] L.C. Kimerling, K.D. Kolenbrander, J. Michel, J. Palm, Solid State Phys. 50 (1997) 333–381.
[10] M. Markmann, A. Sticht, F. Bobe, G. Zandler, K. Brunner, G. Abstreiter, E. Müller, J. Appl. Phys. 91 (2002) 9764–9771.
[11] S. Coffa, S. Libertino, G. Coppola, A. Cutolo, IEEE J. Quantum Electron. 36 (2000) 1206–1213.
[12] M.E. Castagna, S. Coffa, M. Monaco, L. Caristia, A. Messina, R. Mangano, C. Bongiorno, Physica E 16 (2003) 547–553.
[13] G. Franzò, F. Iacona, A. Canino, G. Di Stefano, D. Sanfilippo, A. Piana, P.G. Fallica, F. Priolo, Physica E 38 (2007) 181–187.
[14] Report on silicon industrial investments—indicates that capital expenditure in 2007 will exceed 58.9 billion USD, Friedman Billing Ramsey and Co. Inc., September, 2006.
[15] Compound semiconductor optoelectronics held a 3.6 billion USD market share in 2005, Laser Focus World Magazine, February, 2005.
[16] S. Coffa, F. Franzo, F. Priolo, Mater. Res. Soc. Bull. 23 (1998) 25–32.
[17] D.J. Eaglesham, J. Michel, E.A. Fitzgerald, D.C. Jacobson, J.M. Poate, J.L. Benton, A. Polman, Y.-H. Xie, L.C. Kimerling, Appl. Phys. Lett. 58 (1991) 2797–2799.
[18] A. Polman, J.S. Custer, E. Snoekes, G.N. van den Hoven, Appl. Phys. Lett. 62 (1993) 507–509.
[19] P. Liu, J.P. Zhang, R.J. Wilson, G. Curello, S.S. Rao, P.L.F. Hemment, Appl. Phys. Lett. 66 (1995) 3158–3160.
[20] W.-X. Ni, K.B. Joelsson, C.-X. Du, I.A. Buyanova, G. Pozina, W.M. Chen, G.V. Hansson, B. Monemar, J. Cardenas, B.G. Svensson, Appl. Phys. Lett. 74 (1997) 3383–3385.
[21] J. Stimmer, A. Reittinger, J.F. Nutzel, G. Abstreiter, H. Holzrecher, Ch. Buchal, Appl. Phys. Lett. 68 (1996) 3290–3292.
[22] M. Morse, B. Zheng, J. Palm, X. Duan, L.C. Kimerling, in: S. Coffa, A. Polman, R.N. Schwartz (Eds.), Rare-Earth Doped Semiconductors II. Materials Research Society Symp. Proc., vol. 422, 1996, p. 41.
[23] A. Wang, J. Coffer, Nano Lett. 2 (2002) 1303–1305.
[24] K. Suh, J.H. Shin, O.-H. Park, B.-S. Bae, J.-C. Lee, H.-J. Choi, Appl. Phys. Lett. 86 (2005) 053101-1–053101-3.
[25] B.Y. Tsaur, L.S. Hung, Appl. Phys. Lett. 37 (1980) 922–924.
[26] J.A. Knapp, S.T. Picraux, C.S. Wu, S.S. Lau, J. Appl. Phys. 58 (1985) 3747–3757.
[27] G. Guizzetti, E. Mazzega, M. Michelini, F. Nava, J. Appl. Phys. 67 (1990) 3393–3399.
[28] M.F. Wu, A. Vantomme, H. Pattyn, G. Langouche, Q. Yang, Q. Wang, J. Appl. Phys. 80 (1996) 5713–5717.
[29] M. Jang, J. Oh, S. Maeng, W. Cho, K. Kang, K. Park, Appl. Phys. Lett. 83 (2003) 2611–2613.
[30] S. Salem, Master's Thesis, University of Jordan, 2003.
[31] J.F. Ziegler, SRIM-2003, Nuclear Instruments and Methods in Physics Research Section B: Beam Interactions with Materials and Atoms, 219–220, pp. 1027–1036, 2004, http://www.SRIM.org.
[32] M. Mayer, SIMNRA User's Guide, Max-Planck-Institut für Plasmaphysik, Garching, Germany, 2006, http://www.rzg.mpg.de/~mam.
[33] R.J. Macdonald, E.C. Taglauer, K.R. Wandeldt (Eds.), Surface Science: Principles and Current Applications, Springer, Telos, 1996;
S.A. Abedrabbo, D.E. Arafah, O. Gokce, L.S. Wielunski, M. Gharaibeh, O. Celik, N.M. Ravindra, J. Electron. Mater. 35 (2006) 834–839.
[34] E. Desurvire, Erbium Doped Fiber Amplifiers: Principles and Applications, Wiley, New York, 1994, Chapter 4.
[35] A. Polman, J.S. Custer, E. Snokes, G.N. van den Hoven, Nucl. Instr. Meth. Phys. Res. B 80–81 (1993) 653–658.
[36] E. Desurvire, J.R. Simpson, Optics Lett. 15 (10) (1990) 547–549.
[37] S. Lombardo, S.U. Campisano, G.N. van den Hoven, A. Cacciato, A. Polman, Appl. Phys. Lett. 63 (14) (1993) 1942–1944.
[38] J. Michel, J.L. Benton, R.F. Ferrante, D.C. Jacobson, D.J. Eaglesham, E.A. Fitzgerald, Y.-H. Xie, J.M. Poate, L.C. Kimmerling, J. Appl. Phys. 70 (1991) 2672–2678.
[39] F.Y.G. Ren, J. Michel, Q. Sun-Paduano, B. Zheng, H. Kitagawa, D.C. Jacobson, J.M. Poate, L.C. Kimmerling, in: G.S. Pomrenke, P.B. Klein, D.W. Langer (Eds.), Rare Earth Doped Semiconductors, Mater. Res. Soc. Symp. Proc. 422 (1996) 87.
[40] J. Michel, L.V.C. Assali, M.T. Morse, L.C. Kimerling, Erbium in Silicon, in: D.J. Lockwood (Ed.), Light Emission in Silicon from Physics to Devices. Semiconductors and Semimetals Series, vol. 49, Academic Press, Chestnut Hill MA, 1998, p. 135, Chapter 4.
[41] F.G. Anderson, Appl. Phys. Lett. 68 (17) (1996) 2421–2423.
[42] Optical system design and engineering considerations, in: Series G: Transmission Systems and Media, Digital Systems and Networks, ITU supplement 39, International Telecommunications Union, Geneva, pp. 9–10, http://www.itu.int.
[43] Generic Criteria for SONET Point-to-Point Wavelength Division Multiplexed Systems in the 1550 nm Region, in: Bellcore GR-2918-Core Document, Bellcore, Piscataway, NJ, 1996.
[44] C.C. Robinson, J. non-Cryst. Solids 15 (1) (1974) 1–9.
[45] S.J. Strickler, R.A. Berg, J. Chem. Phys. 37 (4) (1962) 814–822.